Journal of Materials Chemistry A

RSC Publishing

PAPER

View Article Online
View Journal | View Issue

Robust lithium-ion anodes based on nanocomposites of iron oxide–carbon–silicate†

Cite this: *J. Mater. Chem. A*, 2013, **1**, 4539

Received 26th September 2012
Accepted 17th December 2012

DOI: 10.1039/c2ta00443g

www.rsc.org/MaterialsA

Hiesang Sohn,[a] Zheng Chen,[a] Yoon Seok Jung,[b] Qiangfeng Xiao,[c] Mei Cai,*[c] Haiqiang Wang*[d] and Yunfeng Lu*[a]

Robust composite particles containing Fe_3O_4 cores and porous conductive carbon–silicate layers were synthesized using an aerosol-assisted process followed by vapor coating using organosilanol as the precursor. Such unique synthesis enables the composites with high capacity and good cycle performance, and can be extended towards other oxide composites for energy storage.

1 Introduction

Lithium-ion batteries (LIBs) are commonly used for portable electronic devices, and the applications have been expanding for electric vehicles and other devices.[1] Conventional LIBs are operated based on graphite anodes and lithium-metal-oxide cathodes. Graphite exhibits a theoretical capacity of 372 mA h g^{-1}; finding alternative anode materials with higher capacity is essential towards devices with higher energy density.[1,2] In this context, transition-metal oxides (*e.g.*, MO_x, M = Fe, Co, Ni, Cu, and Mo) hold great promise owing to their high theoretical capacities.[2,3] Iron oxides, in particular, are of great interest due to their abundance, environmental benignity and high capacity (*e.g.*, 926 mA h g^{-1} for Fe_3O_4).[1–3] However, similar to other transition-metal oxides, iron oxide exhibits relatively low electronic conductivity and poor cycling stability due to the large volume change during Li insertion–extraction.[3,4]

To date, various approaches have been proposed to improve the cycling stability and rate capability of the metal oxides.[5,6] Forming carbon composites has been a major approach, since the carbon moiety may increase conductivity, reduce aggregation of the oxide particles,[5–11] and mitigate mechanical stress generated during the charge/discharge process.[8] Generally, such composites were synthesized by mixing oxide particles or their precursors with carbon sources (*e.g.*, glucose[3,7] and furfuryl alcohol[7]) followed by the carbonization process. For such a process, high carbonization temperature (*e.g.*, >600 °C) is generally required in order to achieve a good electronic conductivity;[8] however, such a high temperature process often renders the oxides reduced.[8,11] As an alternative approach, the composites can also be made by directly mixing oxide particles with conductive agents, such as porous carbon,[8] carbon nanotube,[9] and graphene.[10] This approach led to improved performances; however, the most previous approaches adopt relatively complex and expensive synthetic procedures which are hard to be scaled up.

Herein, we report a novel synthesis of the nanocomposite of iron oxide, carbon and silicate for high-performance LIB anodes. Our synthesis strategy is to make the mesoporous composite of iron oxide and carbon particles with layers of porous conductive carbon–silicate through an organosilanol

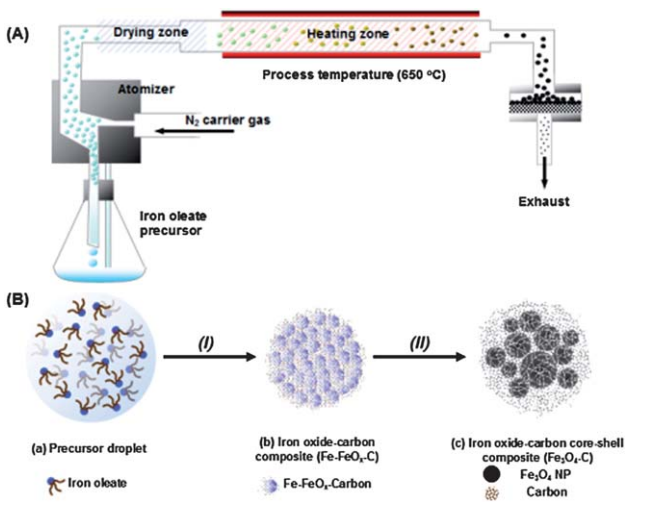

Fig. 1 Scheme of synthesizing Fe_3O_4–C core–shell particles by an (I) aerosol process using iron oleates as precursors followed by a (II) sintering–coating process in the presence of diphenylsilandiol (DPSD): (A) schematic of the aerosol process (B) (a) precursor droplet generated by the aerosol process containing an iron oleate precursor, (b) the aerosol droplets were converted to composite particles of iron oxide and carbon in the heating zone, and (c) formation of porous iron oxide–carbon composite particles with a core–shell after DPSD vapor coating.

[a]*Department of Chemical and Biomolecular Engineering, University of California, Los Angeles, CA 90095, USA. E-mail: luucla@ucla.edu*

[b]*Interdisciplinary School of Green Energy, Ulsan National Institute of Science and Technology (UNIST), Ulsan 689-798, Korea*

[c]*General Motors R&D Center, Warren, Michigan 48090, USA. E-mail: mei.cai@gm.com*

[d]*School of Environmental Engineering, Zhejing University, Hangzhou 310029, China. E-mail: haiqiangwang@zju.edu.cn*

† Electronic supplementary information (ESI) available: Fig. S1–S13 and Table S1. See DOI: 10.1039/c2ta00443g

vapor coating technique. As illustrated in Fig. 1, the synthetic procedure comprises two steps. We first synthesized mesoporous iron–carbon (Fe–FeO_x–C) composite particles using an aerosol-assisted process (Fig. 1A). Iron oleate in toluene was used as the precursor solution; an atomization process using nitrogen as the carrier gas continuously generates aerosol droplets (Fig. 1B-a). The droplets pass through a heating zone and are converted into mesoporous composite particles (Fig. 1B-b) containing carbon and nanocrystals of iron (step I: a and b). These composite particles were then coated with layers of silicate–carbon (Fig. 1B-c) using diphenylsilandiol (DPSD) as the precursor at elevated temperature (*e.g.*, 800 °C) (step II: b and c).

Note that the composition of the as-synthesized mesoporous particles depends on the reactor temperature.[12] It was found that particles synthesized at 450 °C were mainly composed of amorphous FeO_x while those synthesized at 850 °C were mainly composed of α-Fe and FeC_3. A reactor temperature of 650 °C was chosen to synthesize the Fe–FeO_x–C composite particles (Fig. S1†). During the subsequent coating process for the as-formed mesoporous particles, water liberated from the self-condensation reactions of DPSD can further oxidize the Fe–FeO_x nanocrystals into Fe_3O_4.[13] This unique process not only avoids the reduction of FeO_x that might occur in the conventional carbonization process, it also structurally stabilizes the Fe_3O_4 particles with uniform silicate (SiO_x)/carbon coatings. This unique core–shell structure provides critical features needed for high-performance Li-storage. For example, the porous networks enable effective transport of Li ions and electrolyte. The carbon coatings formed at high temperature provide high electronic conductivity. Moreover, the core–shell structure endows the particles with structural robustness and good cycling stability due to its ability to alleviate mechanical stress generated during the charge/discharge process.[4,6]

We noticed that conventional vacuum deposition techniques, such as chemical vapor deposition (CVD)[14] and atomic layer deposition (ALD),[15] as the direct growing method of the active electrode materials for the LIBs require large amount of precursors and expensive facilities. In contrast, the process described here utilized DPSD as the precursor and regular tube furnaces as the coating chamber. Since DPSD is a compound commonly used for the large-scale production of silicon-based materials, the cost of such a precursor is far cheaper than those of the organometallic precursors used for the CVD and ALD processes. Moreover, such a coating process does not require expensive facilities and operating conditions (*e.g.*, low pressure) since the vaporized DPSP above its boiling temperature (~350 °C) allows uniform coating using a regular furnace, thereby enabling the fabrication of a structurally stable oxide–carbon–silicate nanocomposite beyond Fe_3O_4 for lithium-ion storage and other applications.

2 Experimental

Synthesis of composite particles of iron and carbon

The composite particles were synthesized using iron oleate as the precursor. 1.622 g of $FeCl_3$ (Sigma-Aldrich) and 8 mL of oleic acid (Sigma-Aldrich) were dissolved in 100 mL of methanol; then NaOH–methanol solution was dropped into the solution, resulting in a dark brown precipitate. An iron-oleate complex was obtained after solvent evaporation. Iron oleate (3 g) dispersed in toluene (50 mL) was sent through an atomizer using nitrogen as a carrier gas as shown in Fig. 1A.[12,16] The aerosols passed through a ceramic tube heated to 650 °C; as formed composite particles of iron and carbon (denoted as Fe–FeO_x–C) were collected on a filter heated to 80 °C.

Synthesis of Fe_3O_4–carbon core–shell nanocomposite

The composite particles were prepared by thermal treatment of Fe–FeO_x–C in the presence of diphenylsilandiol (DPSD) (Sigma-Aldrich). Typically, 0.1 g of the Fe–FeO_x–C powder in a ceramic boat was placed within a tube furnace, which had an inner volume of 12 cm^3. 1 g of DPSD was placed ~5 cm away from the boat. The furnace was ramped from room temperature to 400 °C and maintained at 400 °C for 1 h, then ramped to 550 °C and maintained at 550 °C for 2 h, and finally ramped to 800 °C and maintained at 800 °C for 2 h under argon flow (1 mL s^{-1}). Fe_3O_4 nanopowder (Fe_3O_4-NP) purchased from Sigma-Aldrich was used without further purification; the coated-Fe_3O_4-NP was prepared by the coating process described above.

Material characterizations

The size and morphology of the Fe_3O_4–C composites were obtained on a FEI CM120 regular transmission electron microscope (TEM) at an accelerating voltage of 100 kV. High-resolution transmission electron microscopy (HR-TEM) images were taken on a field emission microscope JEM-2100F at an accelerating voltage of 200 kV. Scanning transmission electron microscopy (STEM) and elemental maps were carried out using the high-angle annular dark field (HAADF) mode on the same microscope. TEM samples were prepared by dropping the dilute sample solution onto a carbon-coated TEM grid in which solvent (methanol) was evaporated in air. Scanning electron microscopy (SEM) images were obtained with a JEOL 6700 scanning electron microscope at an accelerating voltage of 1.5 kV. The SEM samples were mounted on an aluminium stub with conductive carbon sticky tape. The nanocrystalline structure was analyzed by X-ray diffraction (XRD) using a PANalytical X'Pert PRO System using the Cu K-alpha radiation and fixed source ($\lambda = 0.154056$ nm). Cu K-alpha radiation and a fixed power source (45 kV and 40 mA) were used. The data were collected over a 2θ range between 20 and 80°. Thermogravimetric analysis (TGA) was carried out using a thermogravimetric analyzer (TA instruments) with a heating rate of 10 °C min^{-1} in Ar or in air for thermogravimetric-mass spectrometric analysis. Infrared spectra (FT-IR) were collected using a JASCO infrared spectrometer. The Raman spectra were obtained with a Renishaw Microscope Raman spectrometer using backscattering geometry. Spectra were averaged over 20 accumulations and the laser power was kept at 2.5 mW. Nitrogen sorption isotherms were at 77 K with a Micromeritics ASAP 2020 analyzer (Micromeritics Instrument Corporation, Norcross, GA). Specific surface areas (S_{BET}) were calculated by the

Brunauer–Emmett–Teller (BET) method using the adsorption branch in a relative pressure range from 0.04 to 0.25. The pore size distribution was calculated from desorption branch of the N_2 isotherm using the Barrett–Joyner–Halenda (BJH) method.

Electrochemical characterization

Two-electrode 2032-type coin cells were employed to assess the electrochemical performance of samples (Fe_3O_4-NP, coated-Fe_3O_4-NP, Fe_3O_4–C). The composites (active material) were mixed with carbon black (Alfa Aesar) and poly(vinyl difluoride) (PVDF) in a weight ratio of 80 (active) : 10 (carbon black) : 10 (PVDF), then 1-methyl-2-pyrrolidinone (NMP, Aldrich) was added to form homogeneous slurries. The slurries were pasted onto the copper foils (Alfa Aesar) and dried at 80 °C in a vacuum oven for 12 h. The electrodes were then further annealed at 250 °C under Ar atmosphere overnight. The average mass loadings for all electrodes were about 1.5–2 mg cm^{-2}.

The cells were assembled using 1 M $LiPF_6$ in ethylene carbonate and diethyl carbonate (EC : DEC, v/v = 1 : 1, Merck) as the electrolyte, Celgard 2500 as the separator film. Pure lithium foil (99.9%, Aldrich) was used as the counter electrode and reference electrode. The cells were assembled in an argon-filled glove box, where moisture and oxygen levels were kept below 0.3 ppm. Electrochemical experiments were performed using coin-type cells, which were cycled in the voltage range between 3.0 V and 0.01 V with a battery test system (LAND CT2000: Wuhan Jinnuo Electronics, Ltd., Wuhan, China). The capacity was calculated based on the total mass of composites, including the mass of Fe_3O_4, carbon and silicate. For the cycling stability test, the current rate was set as 0.13 A g^{-1} for the first three cycles and set as 0.5 A g^{-1} for the subsequent 50 cycles. Various current densities were further used to evaluate the rate-capability. Cyclic voltammograms (CVs) measurements were carried out on a Solartron 1860/1287 Electrochemical Interface (Solartron Analytical, Oak Ridge, TN) over the potential range 0.005 to 3.000 V *versus* Li/Li^+ at a scanning rate of 0.2 mV s^{-1}. All cells were tested at room temperature.

3 Results and discussion

To demonstrate the feasibility of this approach, Fig. 2 shows the representative scanning electron microscope (SEM), transmission electron microscope (TEM) and scanning-TEM (STEM) images of the composite particles. The SEM image (Fig. 2a) shows that the composite particles are spherical in shape with polydisperse sub-μm to μm sizes. The inset shows a digital photograph of the particles in the form of powder. The TEM image (Fig. 2b) reveals a highly porous core–shell structure (*ca.* 500 nm) in which *ca.* 100 nm sized agglomerated clusters of Fe_3O_4 nanoparticles are embedded within spongy porous carbon matrix, as further confirmed by the STEM image (Fig. 2d). HR-TEM image (Fig. 2c) suggests that the oxide nanoparticles exhibit a lattice fringe ~0.25 nm, which corresponds to the (311) planes of the Fe_3O_4 crystals. Fig. 2e shows a dark field STEM image of the particles and their elemental mapping of Fe (blue), O (red), and C (green) obtained by energy dispersive X-ray spectroscopy (EDX). These results further confirm the embedment of Fe_3O_4 within the carbon matrix. Their elemental composition (Fe_3O_4 + SiO_x: 83.6 wt%, C: 16.4 wt %) was calculated by thermogravimetric analysis (TGA) as displayed in Fig. S2.† The EDX analysis displays very small amount of Si (0.7 wt%) presenting in the composite (Fig. S3 and

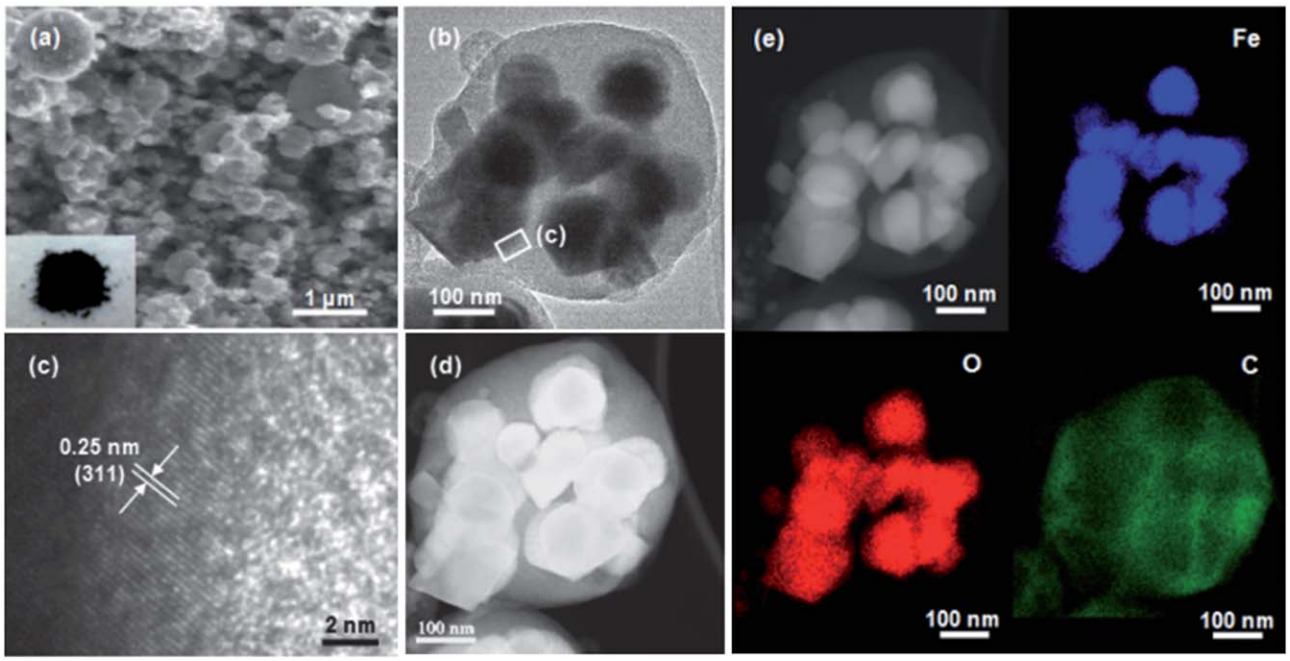

Fig. 2 (a) SEM (inset: digital photograph), (b) TEM, (c) high-resolution TEM, and (d) STEM images of the Fe_3O_4–carbon composite particles. (e) STEM and elemental mapping images of Fe_3O_4–C particles (Fe (blue), O (red), C (green)).

Table S1†). Such a presence of Si unambiguously supports the deposition of silicate–carbon on the porous particles. Note that such a small amount of Si present in the composite as a form of silicate does not contribute to the capacity of the electrode.

Pore structure of the composite particles was further characterized with nitrogen sorption analysis. Fig. S4† shows the nitrogen-sorption isotherms and pore-size distributions of the particles, which suggests the coexistence of micropores and mesopores. As shown in the N_2 adsorption isotherm (Fig. S4a†), the nitrogen-uptake step at the relative pressure (P/P_0) less than 0.2 is mainly contributed by the micropores within the carbon shells. The nitrogen-uptake step at P/P_0 higher than 0.6 was attributed to the mesopores, which were narrowly distributed and centered at ~4 nm (Fig. S4b†). These particles exhibited a high pore volume of 0.217 $cm^3\ g^{-1}$ and BET surface area of 237 $m^2\ g^{-1}$.

The formation of such mesoporous composite particles is attributed to the sintering–coating process in the presence of DPSD. Fig. 3a shows TEM images of particles before and after sintering at 400 °C, 550 °C and 800 °C for 1, 3, and 5 hours, respectively. Prior to the sintering process, the particles were mainly composed of polycrystalline iron (Fe–FeO_x) that forms a three-dimensional mesoporous network.[16] The subsequent sintering process gradually grows the nanocrystals, leading to the formation of Fe_3O_4–carbon/silicate composite particles with a pomegranate-like structure. In consistency with the TEM observation, the particles prior to the sintering process were mainly composed of carbon and Fe in the presence of a small amount of FeO_x, as determined by X-ray photoelectron spectroscopy analysis (XPS) (Fig. S5†). Fig. 3b shows X-ray diffraction (XRD) patterns of the particles before and after the sintering process. The crystallite size of the particles before sintering was around 3 nm by Debye–Scherrer equation. Sintering at 400 °C converted the Fe and FeO_x into Fe_3O_4 with an average size of 8.5 nm. The Fe_3O_4 crystal phase was maintained after the further sintering process at 550 °C and 800 °C, although the crystallite sizes increased from 8.5 nm (400 °C) to 25.1 nm (550 °C) and 30.2 nm (800 °C).

It was found that DPSD played an essential role during the formation of such pomegranate-like structures. Indeed, a sintering process of Fe–FeO_x particles in the absence of DPSD led to the formation of heterogeneous phases of Fe_3O_4, FeO and α-Fe (Fig. S6b†). Moreover, it was found that the sintering process in the absence of DPSD expelled the Fe and FeO_x particles out of the carbon shell (Fig. S6a†). Note that DPSD in argon exhibited a weight loss starting at ~350 °C (boiling point of DPSD) and complete weight loss was observed at ~450 °C with a heating rate of 10 °C min^{-1} (Fig. S7†). During its evaporation process, DPSD may be adsorbed onto the particles surface, forming organosilicate coatings through their self-condensation reactions.[13] Subsequent sintering at elevated temperatures converted the organosilicate coatings into conductive carbon–silicate coatings, which prevented the oxide crystals from getting expelled out of the particles. Simultaneously, the self-condensation reactions among the DPSP generates water, which served as the oxidative agent converting FeO_x and Fe into Fe_3O_4.[17,18]

To further probe the formation process, Raman spectroscopy was used to illustrate the structural transformation during the sintering process (Fig. 3c). The particles prior to the sintering process exhibited mixed phases of α-FeOOH (400, 481 cm^{-1}), Fe_2O_3 (598, 652 cm^{-1}) and poorly crystallized carbon (1310 cm^{-1}, 1584 cm^{-1}). After sintering in the presence of DPSD, the particles exhibited intense oxide peaks, such as those of α-FeOOH (397, 474, 687 cm^{-1}) and Fe_2O_3 (603 cm^{-1}) (sintering at 400 °C) and γ-FeOOH (370, 486 cm^{-1}) and $Fe(OH)_3$ (692 cm^{-1})

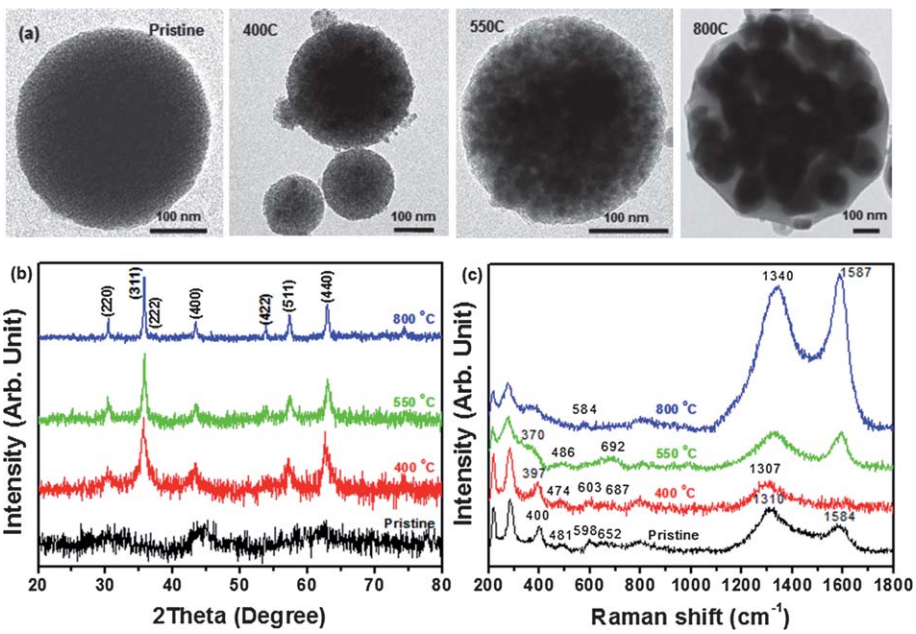

Fig. 3 (a) TEM images, (b) XRD, and (c) Raman spectra of the mesoporous iron-oxide particles sintering in the presence of DPSP at 400, 550 and 800 °C.

(sintering at 550 °C).[18] After the sintering at 800 °C, these oxide species were converted to Fe_3O_4 (584 cm^{-1}), the dominant phase. Moreover, a remarkable enhancement of carbon peak at 1587 cm^{-1} (G-band) was observed after sintering at 800 °C, suggesting the formation of graphitized carbon (sp^2), although the D-band of the carbon is also observed at 1340 cm^{-1}.[19]

Consistent with the Raman spectra, the FT-IR spectrum of the particles sintered at 400 °C in the presence of DPSP shows the adsorption of silanols (Si–OH) and OH between 3000 and 3600 cm^{-1},[20] which became less significant after sintering at 550 °C (Fig. S8†). Such condensation reactions between the surface silanols continuously generates water, contributing to the oxidation of Fe–FeO_x into the oxidized irons (*e.g.*, Fe_2O_3, FeOOH and $Fe(OH)_3$).[20] Furthermore, the characteristic Si–O stretching at 965 cm^{-1} and Si–O–Si stretching at 812 cm^{-1} (550 °C) and 820 cm^{-1} (800 °C) corroborates the formation of carbon–silicate shells.[20] In contrast, the particles sintered without DPSD did not exhibit any Si–O or Si–O–Si stretching (Fig. S9†), further confirming the proposed formation process.

The robust core–shell structure endows the composite particles with outstanding lithium storage property. Galvanostatic charge/discharge was performed to evaluate their storage behavior, as shown in Fig. 4a. The electrodes show voltage profiles with a long plateau at ~0.75 V in discharge (lithiation) and a short plateau at ~1.5 V in the charge (delithiation), which can be ascribed to the overall reaction of $Fe_3O_4 + 8Li^+ + 8e^- \rightarrow 3Fe + 4Li_2O$.[8,10,21] In addition, discharge profiles above 0.7 V can be divided into two segments, *i.e.* a sloping part from 2.0 to 0.75 V, and a plateau at 0.75 V. The former can be attributed to the solid-solution reaction of $Fe_3O_4 + xLi^+ + xe^- \rightarrow Li_xFe_3O_4$ and the latter can be attributed to the conversion reaction of Li_x-$Fe_3O_4 + (8 - x)Li^+ + (8 - x)e^- \rightarrow 3Fe + 4Li_2O$.[22] A positive shift of the plateau on discharge after the first cycle was observed, indicating a crystalline to amorphous structural change.[23] Discharge and charge capacity at first cycle was 1670 and 1090 mA h g^{-1} at a current density of 0.13 A g^{-1}, respectively, rendering relatively low coulombic efficiency (65%). The capacity of higher than the theoretical value (926 mA h g^{-1}) can be attributed to nanosized iron oxide particles and amorphous carbon.[8,24] However, the Fe_3O_4–C composite electrode retained a quite stable capacity of around 900 mA h g^{-1} (Fig. 4b) with near 100% coulombic efficiency (inset in Fig. 4a) in the subsequent 50 cycles, confirming the stable energy-storage capability.

Cyclic voltammetry (CV) measurements (Fig. S10†) also exhibited results consistent with those of voltage profiles. Slight positive shifts (amorphization) of the peak position on the cathodic (−) scan and negatively on the anodic (+) scan were observed after the formation cycle (1st cycle). Nevertheless, the CV profile maintained its initial shape well upon further cycling, suggesting a stable lithium-storage process.

The cycling performance of the Fe_3O_4–C composite was compared with those of control electrodes, Fe_3O_4 nanopowder (Fe_3O_4-NP) and Fe_3O_4-NP with a similar DPSD coating (coated-Fe_3O_4-NP) (Fig. S11†) as displayed in Fig. 4b. The coated-Fe_3O_4-NP showed a much higher reversible capacity than the bare Fe_3O_4-NP (1350 *vs.* 810 mA h g^{-1}) in the initial cycles. Upon

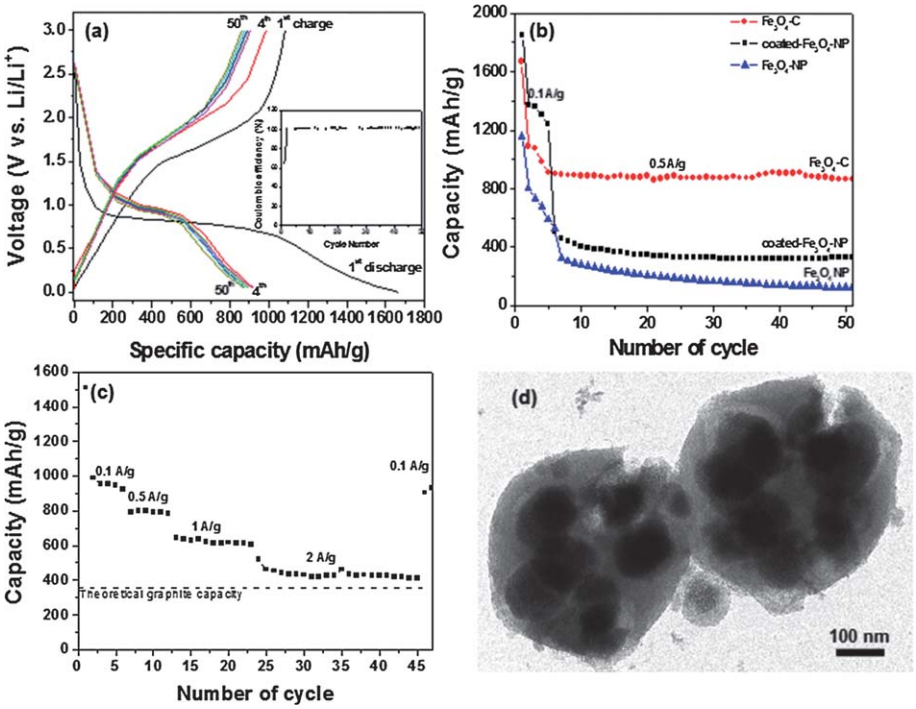

Fig. 4 (a) Voltage profiles of a Fe_3O_4–C composite electrode at a cycling rate of 0.13 A g^{-1} (inset: coulombic efficiency); (b) cycling performance of Fe_3O_4–C composite (Fe_3O_4–C), Fe_3O_4 nanoparticles (Fe_3O_4-NP), and carbon-coated Fe_3O_4-NP nanoparticles (coated-Fe_3O_4-NP) electrode at a cycling rate of 0.13 A g^{-1} for the first 5 cycles and 0.5 A g^{-1} for the subsequent 45 cycles; (c) discharge capacity of a Fe_3O_4–C composite electrode as a function of discharge rate (0.1–2 A g^{-1}); and (d) TEM image of the Fe_3O_4–C composite after 50 cycle at a rate of 0.5 A g^{-1}.

long-term cycling (~50 cycles) the coated-Fe_3O_4-NP also preserved much more capacity than the bare ones (330 *vs.* 115 mA h g^{-1}). This result implies the important contribution of the carbon coatings which improve the electrical conductivity and structural stability, leading to better active material utilization and cycling stability. The composite core–shell particles showed a slightly lower initial capacity than that of the coated-Fe_3O_4-NP due to the less Fe_3O_4 content in the electrodes (Fig. S12†). However, it displayed a much higher capacity (864 mA h g^{-1}) than the coated-Fe_3O_4-NP after 50 cycles. This result suggests that formation of a composite Fe_3O_4–C structure is also critical for the stable electrode structure. Consistently, we also compared the capacity and cycle stability of the carbon–iron-oxide composite particles with and without the coating (Fig. S13†). The coated composite exhibits significantly higher capacity than the uncoated one.

Besides the impressive cycle stability and high capacity, the composite particles also show excellent rate capability as displayed in Fig. 4c. For example, the electrode was cycled under different current densities from 0.1 A g^{-1} to 2 A g^{-1}. At high current densities (*e.g.*, 1 and 2 A g^{-1}), the composite electrodes can still deliver high reversible capacities of 645 and 454 mA h g^{-1}, respectively. Such high-rate performance can be attributed to the good conductivity of the carbon coatings. All of these capacity values are much higher than the theoretical capacity of the already-commercialized graphite (~372 mA h g^{-1}). Remarkably, when the current density was returned to the initial 0.1 A g^{-1} after more than 45 cycles, a capacity of 932 mA h g^{-1} was recovered. Such excellent capacity retention further implies that the core–shell structure plays an important role in maintaining structural integrity of the particles during the charge/discharge process.[10,21] Indeed, after the cycling process, structure and morphology of the composite particles was examined by TEM (Fig. 4d). The particles after the cycling process retained its original core–shell structure, which explains the reason leading to such outstanding performance.

4 Conclusions

In summary, we have demonstrated the synthesis of the composites of iron-oxide and carbon–silicate with a unique core–shell structure by an organosilanol vapor coating technique. Such composite particles exhibit high capacity and good cycle performance, which can be attributed to their unique porous core–shell structure. The formation of such carbon–silicate composites through this CVD-like coating approach can be readily extended to other stable oxide electrodes, enabling the synthesis of a large variety of oxide composites for energy storage and other applications.

Acknowledgements

This work was partially supported by General Motor Inc. (M. C. and Y. L.) and the Molecularly Engineered Energy Materials, an Energy Frontier Research Center funded by the U.S. Department of Energy, Office of Science, Office of Basic Energy Sciences under award DE-SC001342. (Y. L.). This work was also supported by the Energy Efficiency and Resources R&D program (20112010100150) under the Ministry of Knowledge Economy, Republic of Korea (Y. J.). The authors also acknowledge Mr Choong-Heui Chung for the help of Raman Spectroscopy measurements.

Notes and references

1 P. G. Bruce, B. Scrosati and J.-M. Tarascon, *Angew. Chem., Int. Ed.*, 2008, **47**, 2930; A. S. Aricò, P. Bruce, B. Scrosati, J.-M. Tarascon and W. V. Schalkwijk, *Nat. Mater.*, 2005, **4**, 366.
2 P. Poizot, S. Laruelle, S. Grugeon, L. Dupont and J. M. Tarascon, *Nature*, 2000, **407**, 496.
3 M. V. Reddy, T. Yu, C.-H. Sow, Z. X. Shen, C. T. Lim, G. V. S. Rao and B. V. R. Chowdari, *Adv. Funct. Mater.*, 2007, **17**, 2792; X.-L. Wu, Y.-G. Guo, L.-J. Wan and C.-W. Hu, *J. Phys. Chem. C*, 2008, **112**, 16824.
4 Y. Yu, C. H. Chen, J. L. Shui and S. Xie, *Angew. Chem., Int. Ed.*, 2005, **44**, 7085.
5 P. L. Taberna, S. Mitra, P. Poizot, P. Simon and J.-M. Tarascon, *Nat. Mater.*, 2006, **5**, 567.
6 J. Zhou, H. Song, X. Chen, L. Zhi, S. Yang, J. Huo and W. Yang, *Chem. Mater.*, 2009, **21**, 2935.
7 T. Zhu, J. S. Chen and X. W. D. Lou, *J. Phys. Chem. C*, 2011, **115**, 9814; W.-M. Zhang, X.-L. Wu, J.-S. Hu, Y.-G. Guo and L.-J. Wan, *Adv. Funct. Mater.*, 2008, **18**, 3941.
8 E. Kang, Y. S. Jung, A. S. Cavanagh, G.-H. Kim, S. M. George, A. C. Dillon, J. K. Kim and J. Lee, *Adv. Funct. Mater.*, 2011, **21**, 2430.
9 C. Ban, Z. Wu, D. T. Gillaspie, L. Chen, Y. Yan, J. L. Blackburn and A. C. Dillon, *Adv. Mater.*, 2010, **22**, E145.
10 P. Lian, X. Zhu, H. Xiang, Z. Li, W. Yang and H. Wang, *Electrochim. Acta*, 2010, **56**, 834.
11 X.-L. Wu, Y.-G. Guo, L.-J. Wan and C.-W. Hu, *J. Phys. Chem. C*, 2008, **112**, 16824.
12 Q. Xiao, H. Sohn, Z. Chen, D. Toso, M. Mechlenburg, Z. H. Zhou, E. Poirier, A. Dailly, H. Wang, Z. Wu, M. Cai and Y. Lu, *Angew. Chem., Int. Ed.*, 2012, **51**, 10546.
13 T.-H. Lee, J. H. Kim and B.-S. Bae, *J. Mater. Chem.*, 2006, **16**, 1657.
14 A. Magasinki, P. Dixon, B. Hertzberg, A. Kvit, J. Ayala and G. Yushin, *Nat. Mater.*, 2010, **9**, 353.
15 S.-W. Kim, T. H. Han, J. Kim, H. Gwon, H.-S. Moon, S.-W. Kang, S. O. Kim and K. Kang, *ACS Nano*, 2009, **3**, 1085.
16 Y. Lu, H. Fan, A. Stump, T. L. Ward, T. Rieker and C. J. Brinker, *Nature*, 1999, **398**, 223.
17 N. Grassie, K. F. Francey and I. G. Macfarlane, *Polym. Degrad. Stab.*, 1980, **2**, 67.
18 P. Hu, S. Zhang, H. Wang, D. Pan, J. Tian, Z. Tang and A. A. Volinsky, *J. Alloys Compd.*, 2011, **509**, 2316; H. Wang, P. Hu, D. Pan, J. Tian, S. Zhang and A. A. Volinsky, *J. Alloys Compd.*, 2010, **502**, 338.
19 R. J. Thibeau, C. W. Brown and R. H. Heidersbach, *Appl. Spectrosc.*, 1978, **32**, 532; A. C. Ferrari and J. Robertson, *Phys. Rev. B: Condens. Matter*, 2000, **61**, 14095; G. Katumba, B. W. Mwakikunga and T. R. Mothibinyane, *Nanoscale Res.*

Lett., 2008, **3**(11), 421; J. Schwan, S. Ulrich, V. Batori, H. Ehrhardt and S. R. P. Silva, *J. Appl. Phys.*, 1996, **80**, 440.

20 K. H. Jung and B.-S. Bae, *J. Appl. Polym. Sci.*, 2008, **108**, 3169; P. Komadel, J. Madejova, M. Janek, W. P. Gates, R. J. Kirkpatrick and J. W. Stucki, *Clays Clay Miner.*, 1996, **44**, 228; T. T. Baby and S. Ramaprabhu, *Talanta*, 2010, **80**, 2016; B. Shokri, M. Abbasi Firouzjah and S. I. Hosseini, *ISPC Proceeding*, ISPC Conference (ISPC-19), 2009.

21 H. Liu, G. Wang, J. Wang and D. Wexler, *Electrochem. Commun.*, 2008, **10**, 1879.

22 L. Wang, Y. Yu, P. C. Chen, D. W. Zhang and C. H. Chen, *J. Power Sources*, 2008, **183**, 717.

23 J. H. Ku, Y. S. Jung, K. T. Lee, C. H. Kim and S. M. Oh, *J. Electrochem. Soc.*, 2009, **156**, A688.

24 P. G. Bruce, *Solid State Ionics*, 2008, **179**, 752; M. Park, X. Zhang, M. Chung, G. B. Less and A. M. Sastry, *J. Power Sources*, 2010, **195**, 7904.